

Aerothermodynamics modelling of complex shapes in the DEBRISK atmospheric reentry tool: Methodology and validation



Julien Annaloro^{a,*}, Stéphane Galera^b, Cédric Thiebaut^c, Martin Spel^d, Pierre Van Hauwaert^e, Guillaume Grossir^f, Sébastien Paris^f, Olivier Chazot^f, Pierre Omaly^a

^a Orbital Systems Direction, Centre National d'Etudes Spatiales, Toulouse, France

^b ALTRAN Sud-Ouest, Toulouse, France

^c Launch Vehicle Direction, Centre National d'Etudes Spatiales, Paris, France

^d R.TECH, Verviers, France

^e R.TECH, Weesp, the Netherlands

^f Aeronautic and Aerospace department, von Karman Institute for Fluid Dynamics, Rhode-Saint-Genèse, Belgium

ARTICLE INFO

Keywords:

Atmospheric reentry

Debris

DEBRISK

Aerothermodynamics

French space operation act

ABSTRACT

To predict the debris survivability during an atmospheric re-entry and assess the prospective risk on ground, CNES develops an engineering tool named DEBRISK, based on an object-oriented approach. This approach is currently limited to primitive shapes and is therefore difficult to apply to more complex shapes. The objective of this work is to present a new methodology, based on the MISTRAL software, to introduce more complex shapes within DEBRISK with the goal to deal accurately with the atmospheric re-entry of more realistic objects. Moreover, this new methodology is validated by setting up an experimental campaign performed in the Von Karman Institute Longshot wind tunnel.

1. Introduction

Since 1957 and the launch of Sputnik-1, an amazing quantity of human-made objects have reached Earth orbits [1,2]. This amount of debris in Earth orbit, occurs either from the collision between vehicles, or from accidental (or not) break-up failures and also from launch vehicle stages or spacecraft, which have not been removed from orbit after their operational life. Their growing population represents a significant risk for the success of any other operational space mission. Mitigation is therefore required and de-orbitation is recommended by Ref. [3–7]: at the end of the active life, GEO satellites need to be moved to a safe long-term orbit, and LEO ones need to be removed by re-entering the Earth's atmosphere. However, the atmospheric re-entry of debris poses significant risks. Debris fragments that survive and reach the surface of the Earth represent an impact risk to people and property. A number of existing guidelines and regulations use the probability 10^{-4} as the threshold for the re-entry casualty risk [5–8]. Specifically, in France, the French Space Operation Act (LOS) was signed in 2008. CNES is in charge of ensuring the right application of the law by

evaluating the prospective risk. In order to evaluate this risk on ground from debris generated by the atmospheric re-entry of space vehicles, CNES develops its own certification tool named DEBRISK [9,10].

DEBRISK is based on an object-oriented approach. The main idea of this approach is to simplify the vehicle geometry from the break-up altitude into individual simple shapes, defined by the user. The trajectory, the thermal heat load and the possible ablation processes are computed for each fragment. Finally, the demise altitude or the casualty area (in case of survivability) is provided. Most methods implemented within DEBRISK to compute drag forces and thermal heat fluxes are based on engineering methods developed in the 60's [11] and used as well in similar tools (e.g. ORSAT [12], DRAMA [13]).

For all these kinds of tools, whenever a debris with a complex geometry needs to be modelled, an analogy is usually made with one of the primitives available: usually spheres, cylinders, boxes/flat plates (see, Fig. 1). This approach suffers from simplifying assumptions and results in large uncertainties on the survivability calculations. The objective of this paper is to present a new and innovative methodology to introduce more complex shapes within object-oriented tools like

Abbreviations: CNES, Centre National d'Etudes Spatiales (*in French*); LOS, Loi sur les Opérations Spatiales (*in French*), French Space Operation Act (*in English*); CFD, Computational Fluid Dynamics; VKI, Von Karman Institute

* Corresponding author.

julien.annaloro@cnes.fr", 0,0,2

>julien.annaloro@cnes.fr (J. Annaloro).

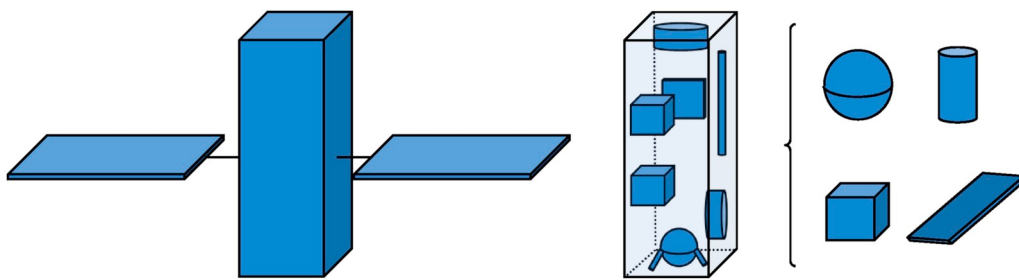


Fig. 1. Simplification and decomposition of a satellite with available primary shape.

DEBRISK. This new methodology is now implemented and available within the version 3 of DEBRISK [10].

For this paper, the first chapter presents the implementation of this methodology, consisting in setting up a CFD numerical database from which aerodynamics and aerothermodynamics models are derived using interpolation schemes. In order to validate this methodology, the second chapter presents experiments carried out in the VKI Longshot hypersonic tunnel using hollow cylinders and hemispherical shells. Aerodynamic coefficients are determined for a wide range of attitudes using a non-intrusive free-flight technique. Local pressure coefficients and heat fluxes are also measured, from which the total power received by the objects is estimated. The last chapter is devoted to the comparison between CFD numerical results with the experimental data obtained and the validation of the methodology.

2. Implementation of an aerothermodynamics database for complex shapes

As for the simple shapes already available in DEBRISK, the survivability analysis of complex shapes requires to compute along the entire trajectory of atmospheric reentry:

- The drag force F_D (N),
- The convective heat flux Q_c (W),
- The radiative heat flux Q_R (W)
- The mass reduction and associated shape modification during the ablation process

Six new topologies are introduced in DEBRISK: open cylinders, open truncated cones, spherical caps as well as the angular sectors of these three shapes (cf. Fig. 2). The modelling of these topologies is based on the implementation of a reduced aerodynamic model for the

determination of the drag force and a reduced aerothermodynamics model for the determination of the convective heat flux. In this paper we only deal with the hypersonic and continuum regime. Model reduction for the entire rarefied regime (transitional and free molecular regimes) will be the subject of other papers. The methodology consists in setting up a CFD numerical database from which the drag force and the convective heat flux are derived using interpolation schemes.

2.1. Dimensionless quantities of interest

The dimensionless form of the drag force and the convective heat flux is necessary. The quantities of interest retained for the CFD numerical database construction are the following:

$$K = \frac{Q}{q_{adim} S_{ref}} \quad (1)$$

$$C_d = \frac{F_D}{q_\infty S_{ref}} \quad (2)$$

with:

- K , the shape factor.
- C_d , the drag coefficient.
- q_{adim} , the stagnation convective heat flux for a sphere of equivalent radius, R_{eq} .
- q_∞ , the dynamic pressure.
- S_{ref} , the reference surface.

An extensive study on the definition of the reference surface and the equivalent radius have been performed in order to have normalized values of K and C_d in the order of unity. This is of major importance since the more the values are uniform, the less error is made in the

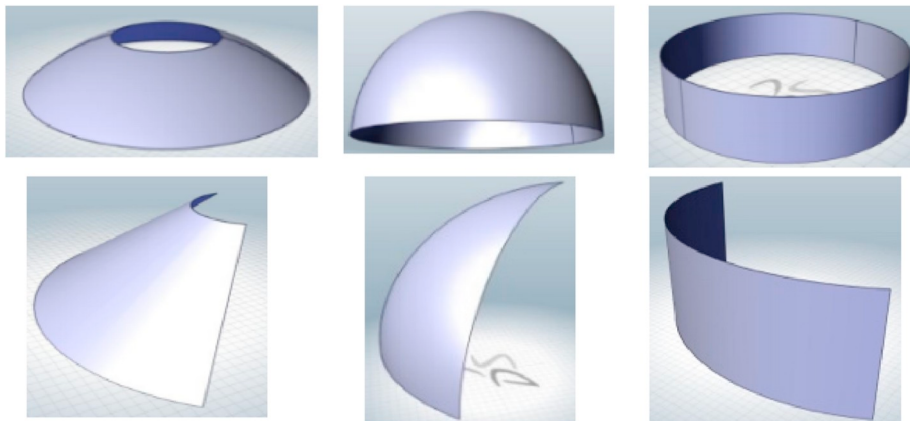


Fig. 2. New shapes available in DEBRISK.

interpolation scheme.

Working with these two quantities of interest makes the interpolation methodology more robust for the following reasons:

- 1 Working directly with the drag force and the convective heat flux provide values with too large orders of magnitude,
- 2 K and C_d are invariant according to the Mach number for the hypersonic and continuum regime,
- 3 K and C_d are invariant for a shape undergoing a homothetic transformation on its geometry.

2.2. Database dimension: geometric parameters reduction

All the six new topologies can be described by a unique set of six geometric parameters: the large radius; the small radius, the height, the thickness, the revolution angle and the flatness (conical or spherical type). Consequently, the drag coefficient and shapes factor would normally be defined by a 6-dimension database.

However, the weak impact of the profile curvature for this type of shape on K and C_d has been demonstrated by a complementary study. This makes it possible to assimilate a shape with a spherical profile to a shape with a linear profile and thus to reduce by 1 the dimension number of the database. In addition, in order to take advantage of the invariance of K and C_d for a defined object by a homothetic transformation, one of the geometric parameters plays the role of a scale factor and normalizes the non dimensionless geometric parameters. Finally, only a set of 4 parameters – in comparison with 6 initially – is used in the building of the database defining the complex shapes.

2.3. CFD numerical database construction

This subsection enumerates the different steps leading to the construction of the K and C_d databases.

- 1 For these two databases, a 4-dimensional cartesian grid is used. Each of the 4 dimension is used for one of the 4 dimensionless geometric parameters (section 2.2).
- 2 The minimum and maximum values of these 4 dimensionless geometric parameters (named L1, L2, L3 and L4 afterwards) represent the domain of definition of the database. It is also named the “bounding box” of the 2 databases (red circles in Fig. 3).
- 3 The 2 databases are respectively built using the quantities of interest K and C_d , resulting from CFD computations. CFD computations are

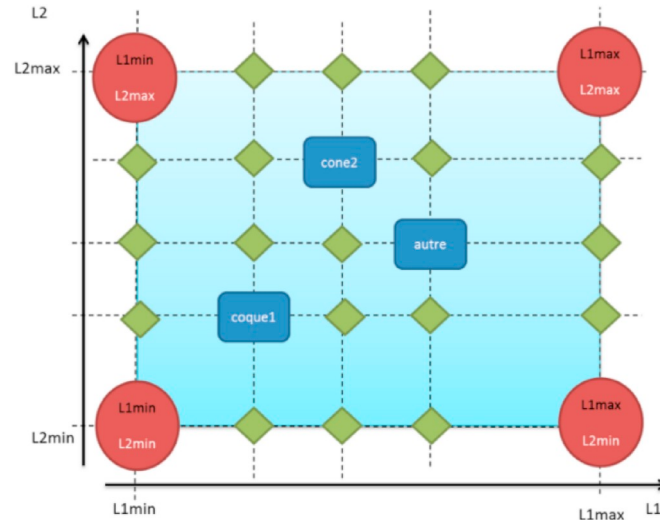


Fig. 3. Schematization of the numerical database with only 2 geometric parameters L1, L2 (for the comprehension of the reader).

performed at the boundaries of the domain, i.e. the *bounding box*. Blue rectangles represent CFD computations within the domain, many of them being chosen where relatively large variations on the quantities of interest are observed.

- 4 The green diamonds are data points required for the multilinear interpolation method. These points are also called *inserts* and are used to complete the missing points of the cartesian mesh. They are generated by interpolation via the inverse distance weighting method from a reduced set of points defined above (red circles + blue rectangles, Fig. 3).

2.4. Quantities of interest interpolation

The different steps for interpolating and computing the convective heat flux and the drag force from the 2 databases, are described below:

- 1 For a given complex shape characterized by these 6 geometrical quantities, the set of normalized (or dimensionless) parameters L1, L2, L3, L4 are computed.
- 2 The interpolated drag coefficient and shape factor (noted \tilde{C}_D et \tilde{K}) for a given complex shape have to be computed from the database (see orange pentagons in Fig. 4). Two cases are to be considered. The first case is when the point to interpolate is within the limits of the bounding box. A quadrilinear interpolation using the $2^4 = 16$ points of the grid surrounding the points (yellow circles in Fig. 4) is carried out. In the other (second) case, an extrapolation (clipping) is carried out. The set of parameters L1, L2, L3 or L4 that will be used as the point to interpolate is the one laying on the boundaries of the database and whose distance to the initial dataset is minimal (see purple pentagon in Fig. 4).
- 3 Once \tilde{C}_D et \tilde{K} are interpolated, the drag force and convective heat flux are rebuilt such as:

$$F_D = \tilde{C}_D q_\infty S_{ref} \quad (3)$$

$$Q = \tilde{K} q_{adim} S_{ref} \quad (4)$$

It should be noted that the implementation in Debrisk supports general N -dimensional geometrical descriptions to allow both applying the methods to more simple shapes such as cylinders and boxes, as well as extending the method to future, more elaborate, objects.

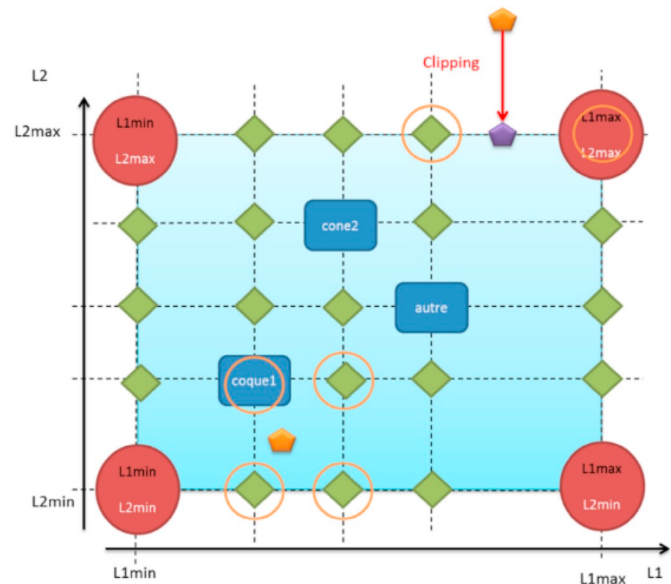


Fig. 4. Schematization of the interpolation method on the normalized database with only 2 geometric parameters L1, L2 (for the comprehension of the reader).

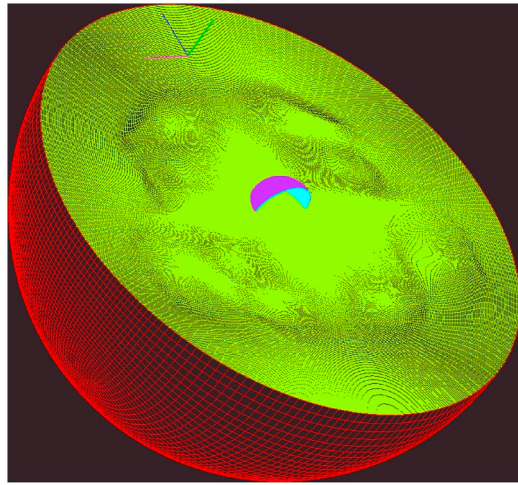


Fig. 5. Spherical inflow/outflow domain.

2.5. Rotating mesh methodology for CFD computations

As for the classical shapes of DEBRISK, the attitude of complex shapes is assumed to be in a random tumbling movement. The CFD computation campaign is performed using an innovative method developed to take into account this specific movement. The purpose of this methodology is to reduce time-consuming step of the mesh generation for each attitude. The method is based on the creation of a single coarse mesh, which is called “spherical mesh”, or “rotating mesh”, Fig. 5, Fig. 6 and Fig. 7.

Through this unique mesh, a large number of simulation points of view (attitude) are placed in a uniform way as shown in Fig. 8. Each point of view corresponds to a CFD simulation with the MISTRAL software for a single direction (attitude) of flow. This approach eliminates the multiple mesh generations – one for each attitude – while maintaining the accuracy. For those purposes a supersonic inflow/outflow boundary condition has been implemented in MISTRAL.

For every CFD computations performed, the drag force F_D and the convective heat flux Q are computed. For each object, a tumbling average is then made using the attitudes (~ 19 for axisymmetric objects, 50 for general objects) accounting for a random-tumbling motion. Over 3000 CFD computations were performed via this methodology in order to feed the 2 databases. This database can be used in the hypersonic regime and for a wide range of geometrical parameters describing the six new topologies.

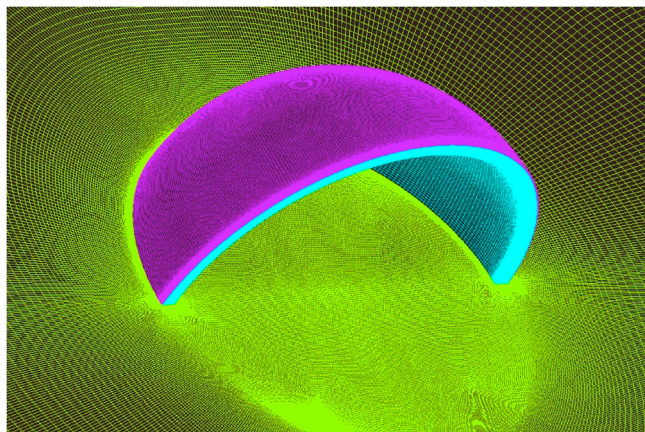


Fig. 6. High density mesh around hollow hemisphere.

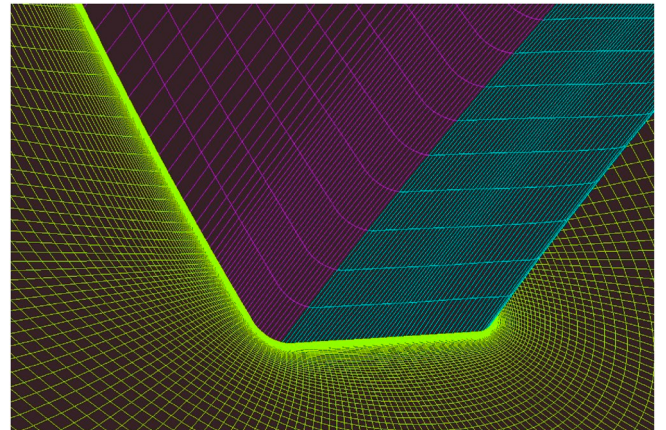


Fig. 7. Close up around corners of hollow hemisphere.

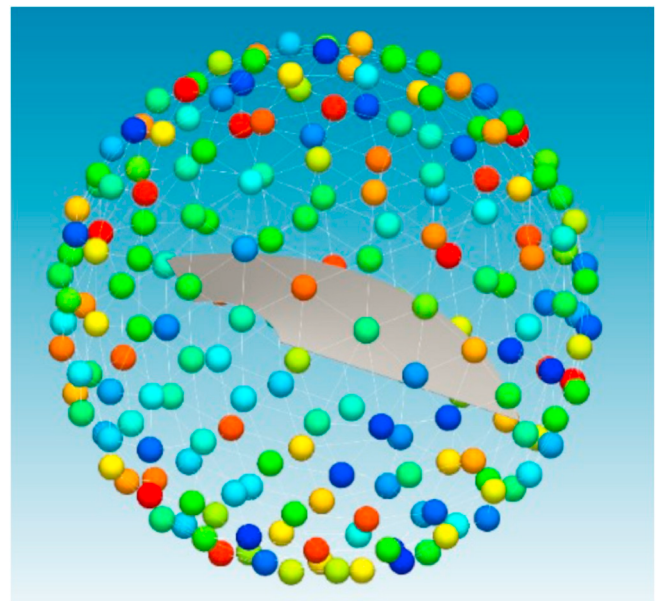


Fig. 8. Distribution of simulation points of view around a shape.

3. Experimental investigations

3.1. Objectives

Hypersonic experiments are performed in a ground facility using different scaled models. The purpose is to determine the aerodynamic coefficients of these geometries, local heat transfer coefficients and local wall pressure coefficients that can be used to validate the numerical results obtained with the rotating mesh approach described in §2.5.

3.2. The VKI longshot hypersonic gun tunnel

The VKI Longshot facility illustrated in Fig. 9 is a hypersonic gun tunnel operated at the von Karman Institute for Fluid Dynamics, in Belgium. It is established as a reference European facility for aerothermodynamic investigations in low-enthalpy perfect gas environments. This wind tunnel is able to generate flows at high Mach numbers (Mach 10–20) together with the large Reynolds numbers pertaining to most of Earth reentry trajectories, including the ones followed by space debris.

This wind tunnel benefits from state-of-the-art flow characterization

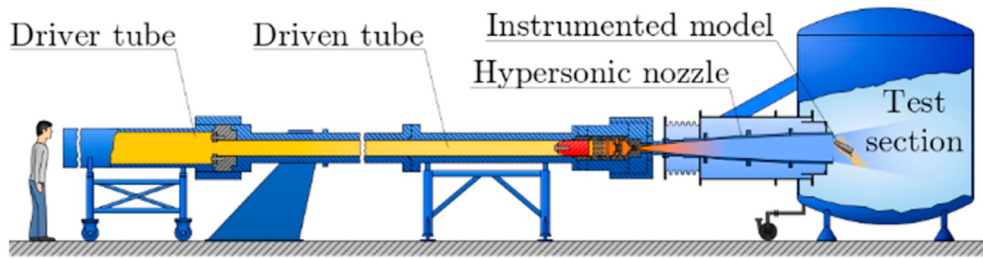


Fig. 9. Sketch of the VKI Longshot hypersonic tunnel.

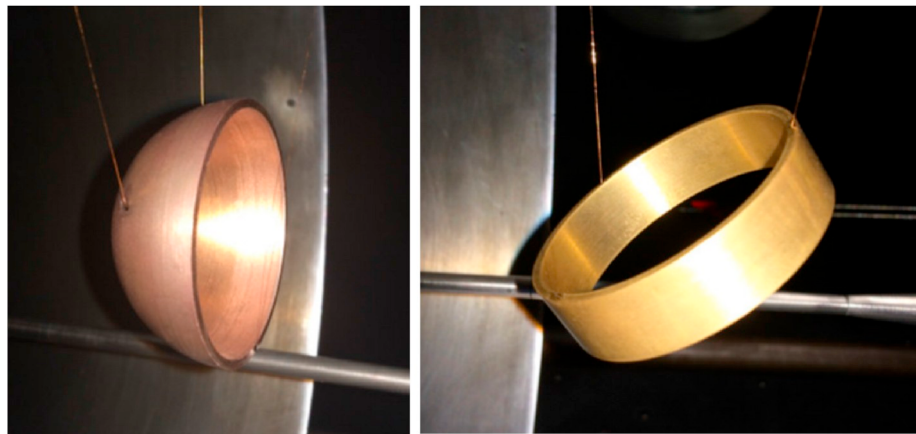


Fig. 10. Scaled models (hollow hemisphere and annular ring) tested in the VKI Longshot tunnel.

methods detailed in Ref. [14] and is therefore particularly well-suited for the present validation of a novel numerical approach.

3.3. Geometries selected for wind tunnel experiments

Geometries of interest were identified based on the specific flow features they would exhibit for some re-entry attitudes. Attached shock waves, shock-shock interactions, shock-boundary layer interactions, flows over concave surfaces, or unsteady flows configurations were deemed particularly interesting to challenge the numerical code.

Among a panel of geometries, two have been selected for the experimental investigations: a hollow hemisphere (typically representing a propellant reservoir split in two), and an annular ring with an aspect ratio of 1/4th (corresponding to a rocket interstage fairing). Both geometries are illustrated in Fig. 10. They present the different flow features of interest (shock-interactions configurations and concave surfaces leading to unsteady flow phenomena). They also have symmetry planes which advantageously reduces the total number of experiments required to cover the entire range of their potential reentry attitudes.

3.4. Test matrices

A total number of 31 experiments are performed in the VKI Longshot tunnel using a contoured nozzle with an exit diameter of 426 mm. It provides a uniform flow field at Mach 11 with a useful test time on the order of 20 ms. Pure nitrogen is used as a test gas for the present experiments which prevents the onset of chemical reactions given the moderate specific stagnation enthalpies which are involved ($< 3 \text{ MJ/kg}$).

Longshot operating conditions are selected in order to match both

Mach and Reynolds numbers (two major similarity parameters for aerothermodynamics investigations) as experienced by space debris during their re-entries, as illustrated in Fig. 11. Representative Longshot free-stream flow conditions for these investigations are given in Table 1.

15 Longshot runs are dedicated to aerodynamic investigations using the free-flight measurement technique described in Ref. [15]. This approach is particularly well-suited for the aerodynamic characterization

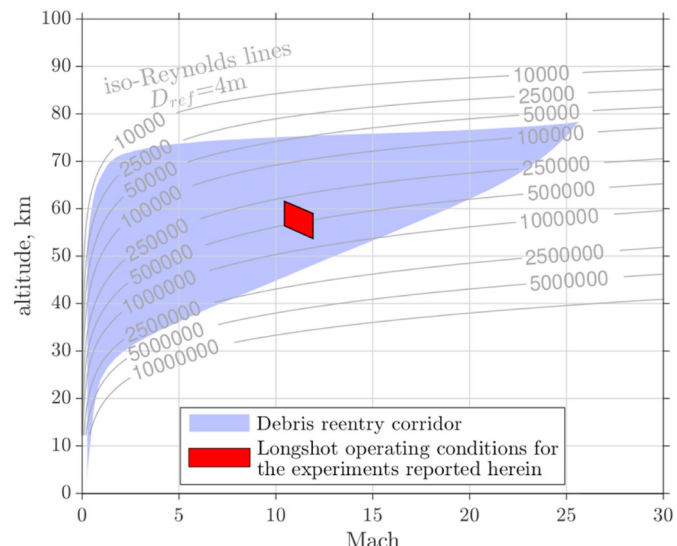


Fig. 11. Re-entry corridor for space debris and selected Longshot flow conditions for the experiments reported herein.

Table 1
Representative Longshot free-stream flow conditions.

Free-stream Mach number, M_{∞}	11.5
Free-stream Reynolds Number, $Re_{D,\infty}$	540000
Free-stream velocity, u_{∞}	2043 m/s
Free-stream pressure, p_{∞}	565.2 Pa
Free-stream temperature, T_{∞}	76.0 K

of space debris which exhibit small internal volume and a wide range of potential re-entry attitudes. Models are automatically released within the hypersonic flow and their motion is tracked using a Schlieren flow visualisation technique and a high-speed camera. Subsequent analysis of the digital images enables to determine the instantaneous aerodynamic coefficients of the objects during their free-flights.

The next 16 Longshot runs are performed on the same geometries, but fixed within the test section, and equipped with instrumentation. They include 15 fast-response coaxial thermocouples from which the local wall heat fluxes are determined. 15 pressure sensors are also distributed over each model. The thermocouples and pressure sensor have been placed at locations where the most complex flow physics is expected (based on preliminary numerical computations). The range for the sensors has been designed accordingly. For the hemispherical model, 26 of these sensors are localized along the concave surface, which is regarded as the most interesting one (Fig. 12). For the annular model, sensors are distributed evenly among the concave and convex surfaces (Fig. 13). The thin edges of the models are not instrumented.

The angle of attack for these models is defined from Fig. 14.

4. Validation of the numerical results

4.1. Numerical tools

The MISTRAL suite of aerothermodynamics codes developed by R.Tech contains both a CFD code and a DSMC code. In this work the MISTRAL-CFD solver has been used. While MISTRAL is capable of thermochemical non-equilibrium modelling, in this work the perfect gas model has been used since the temperatures remain moderate and only slight dissociation is expected. A block structured grid approach is used, distributing blocks over the available processors, allowing for an efficient parallelisation.

Both the free flight experiments and the instrumented experiments have been rebuilt. The variations in angle of attack are performed in steps of 5°. For the hollow sphere the angles range from -90° to 90°, while for the annular ring the angles span from 0° to 90°.

The baseline CFD simulations do not include the sting, allowing the mesh to be identical for all angles of attack. The same meshing approach is therefore used for the experimental rebuilding as the one used for the DEBRISK database generation. For some cases the sting effects have been evaluated and have been found negligible for the integrated heat load.

The first CFD campaign has been performed with estimations of the free stream conditions in order to design the experiments. The choice of pressure sensor locations are sensor ranges have been decided after this

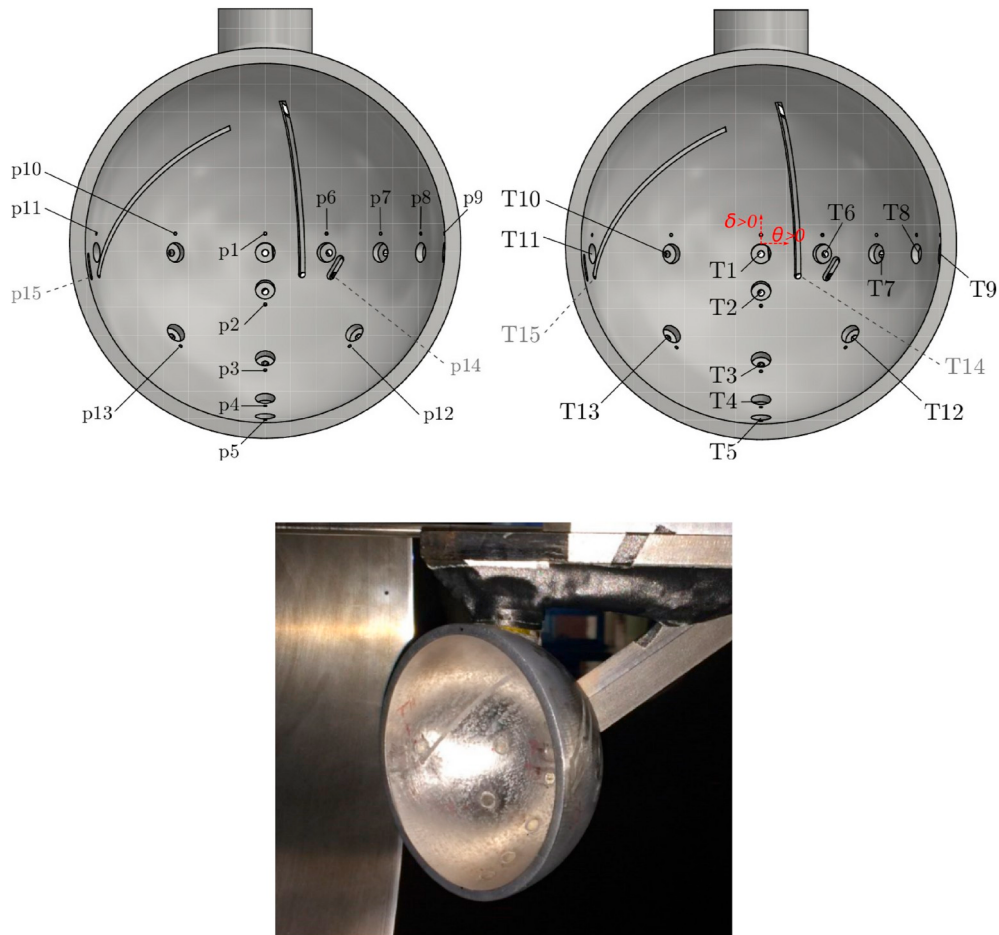


Fig. 12. Instrumented location on the hemispherical model.

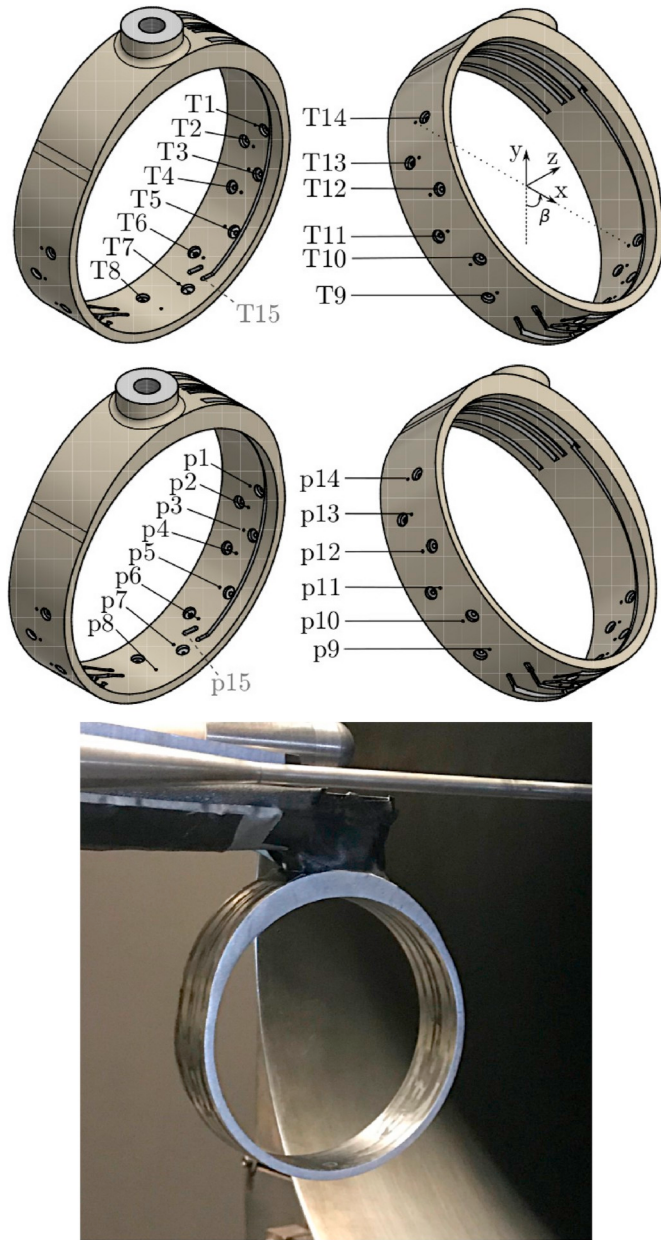


Fig. 13. Instrumented locations on the annular model.

initial design campaign. It was noted that quite high C_p and heat flux values could be obtained, exceeding by far the stagnation point values in case of shock-shock interactions.

The second campaign consisted in a more detailed rebuilding using the flow conditions derived after the experiments.

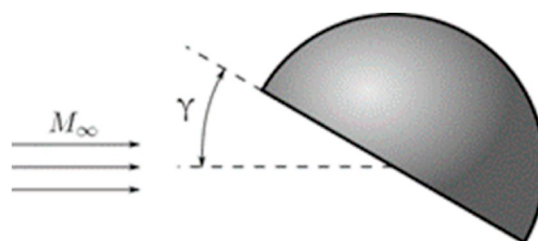


Fig. 14. Convention used for the angle of attack.

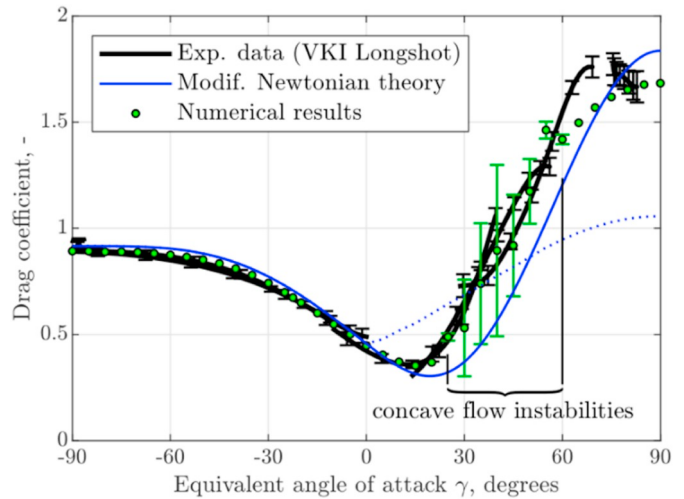


Fig. 15. Drag coefficient for a hypersonic hollow hemisphere for different angles of attack.

4.2. Aerodynamics

4.2.1. Hollow hemisphere

Experimental data obtained in the VKI Longshot tunnel for the hypersonic aerodynamics of a hemisphere are presented in Fig. 15 and Fig. 16 using thick black lines. Free-flight models are successively released at different angles of attack and are then free to adjust to new attitudes depending on the aerodynamic forces which are exerted on them. This enables to cover a wide range of attitudes using only a few

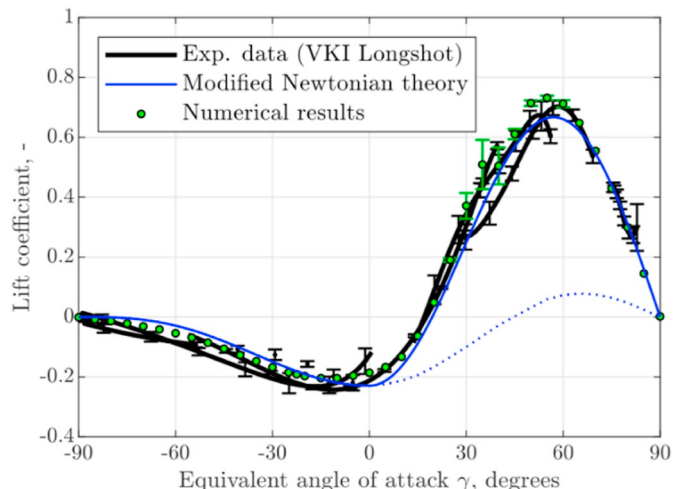


Fig. 16. Lift coefficient for a hypersonic hollow hemisphere for different angles of attack.

Table 2
Averaged drag coefficient for the hollow hemisphere.

Cd _{avg}	
Experimental value	0.762
Numerical value	0.744
Discrepancy (%)	2.5

experimental runs.

Numerical predictions are in good agreement with experimental results, including also the attitudes ($25^\circ < \gamma < 60^\circ$) for which unsteady flows are present over the hemispherical model as it exposes its

concave surface to the incoming flow. The origin of the discrepancies on the drag coefficient observed for angles of attack larger than 60° is not identified yet. The individual angles have been integrated in order to obtain the random tumbling averaged drag coefficient (see Table 2). The numerical value is very close with the experimental value for the hollow sphere.

Theoretical results obtained with the modified Newtonian theory are also included for completeness: the dashed blue curve was obtained assuming a hollow hemisphere and it is shown that this fails to capture the aerodynamics of the object once its concave surface is exposed to the flow. On the other hand, the plain blue curve corresponds to a filled geometry, and enables to better approximate both the experimental and numerical data.

On Fig. 17 a comparison between the Schlieren visualisation is

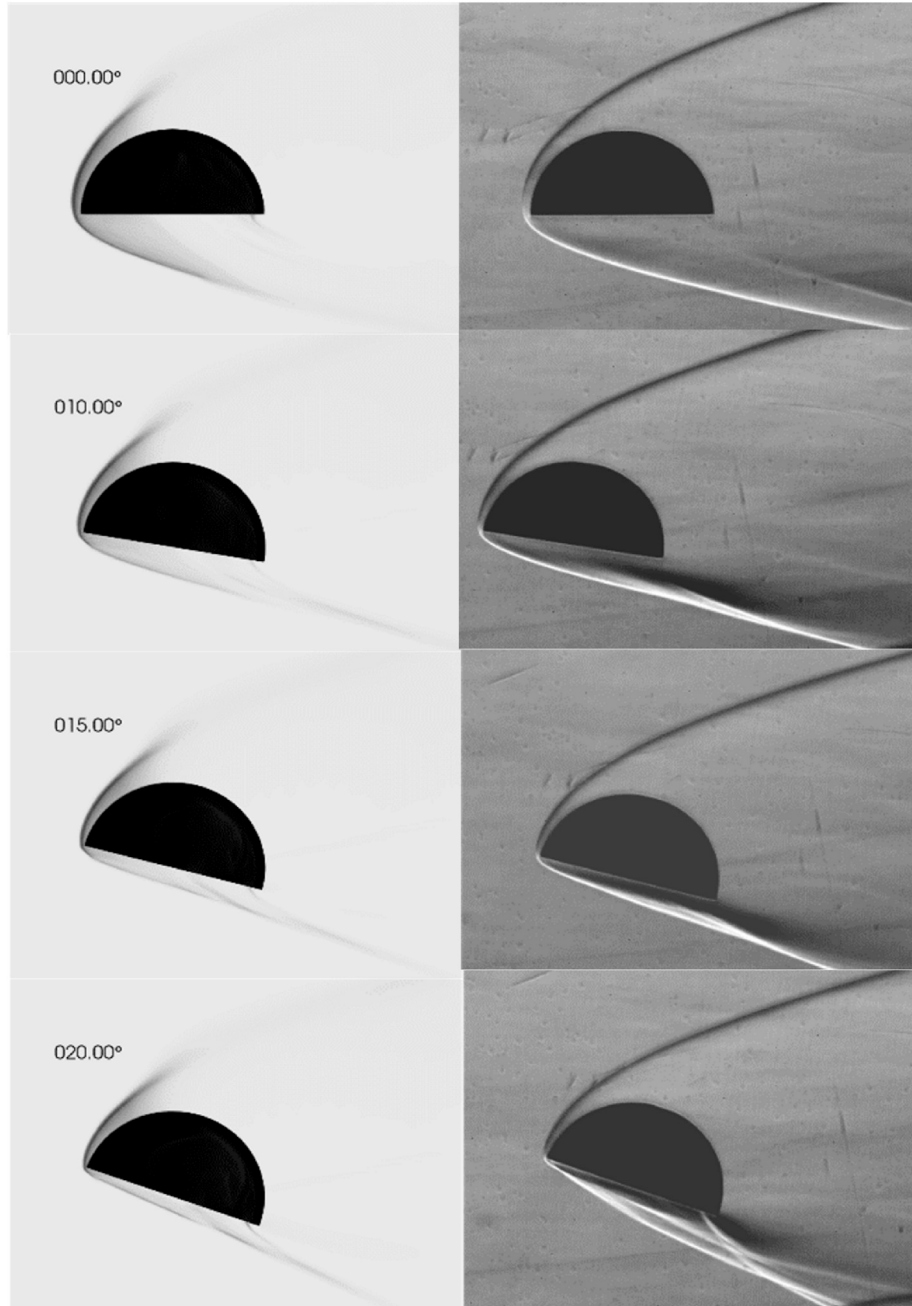


Fig. 17. Schlieren CFD (L) vs experiment (R).

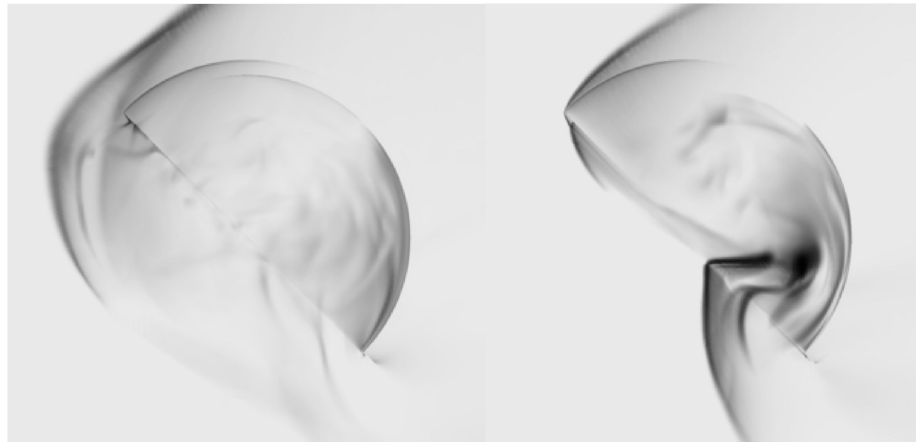


Fig. 18. Numerical Schlieren for the 45° case.

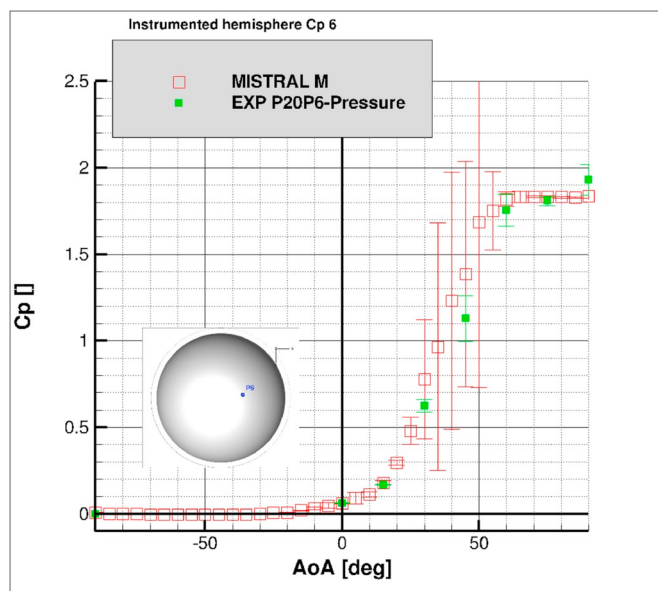


Fig. 19. Surface pressure on downstream point interior of the hollow sphere.

presented for some of the stable angles of attack. An excellent agreement is observed in terms of flow features and shock position, taking into account that the experiments are for free flight, while the CFD computations are performed at a constant angle. Eventual flow hysteresis is therefore not taken into account in the CFD computations.

The Schlieren allow to analyse the unsteady phenomena observed for some angles of attack. For example, in Fig. 18 two distinct instances for the 45° case are highlighted. On the left hand side of the image the shock is detached, lowering the pressure inside the hemisphere. Due to the lower pressure inside the hemisphere, the shock approaches the wall to form an attached shock, shown on the right hand side of the image. The bow shock impacts the aft part of the sphere, resulting in a complex 3D shock wave interaction, which increases the pressure inside the hemisphere. The increased pressure pushes away the shock to the detached state.

In the figures above (Fig. 19, Fig. 20 and Fig. 21) the surface pressures on the hollow sphere are shown for various angles of attack and for three different points. A time averaging is applied and the variations of the signal are plotted as error bars (1 sigma). A very good agreement is observed for the flow angles where no unsteady effects are observed. For the unsteady conditions the amplitude of the variation is larger in the CFD computations than in the experiments, but the mean value is corresponding well to the experimental values.

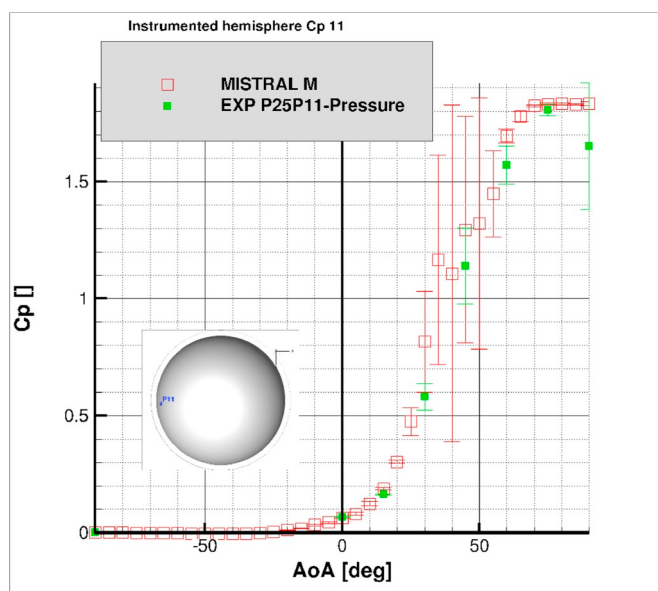


Fig. 20. Surface pressure on upstream point interior of the hollow sphere.

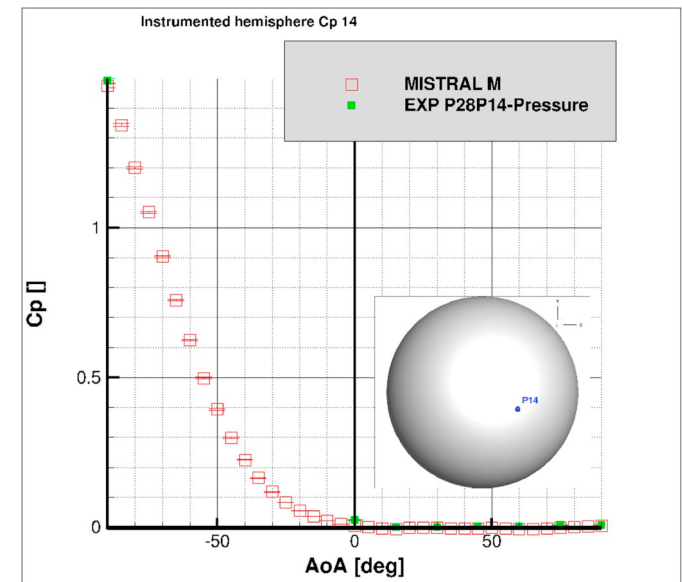


Fig. 21. Surface pressure on exterior of the hollow sphere.

4.2.2. Annular ring

Similar results are presented for the annular ring in Fig. 23 and Fig. 24. This geometry is much more stable than the previous one and free-flight experiments with angles of attack beyond 25° could only be covered for rather discrete values. The numerical predictions are again in good agreement with the experiments which indicates that the

pressure distribution along the different objects is predicted correctly. Newtonian results are included again but fail to match the experimental observations. This is expected given the shock interactions taking place on the geometry. For this geometry as well the flow physics are well captured as seen in the Schlieren visualisation Fig. 22.

The individual angles have been integrated in order to obtain the

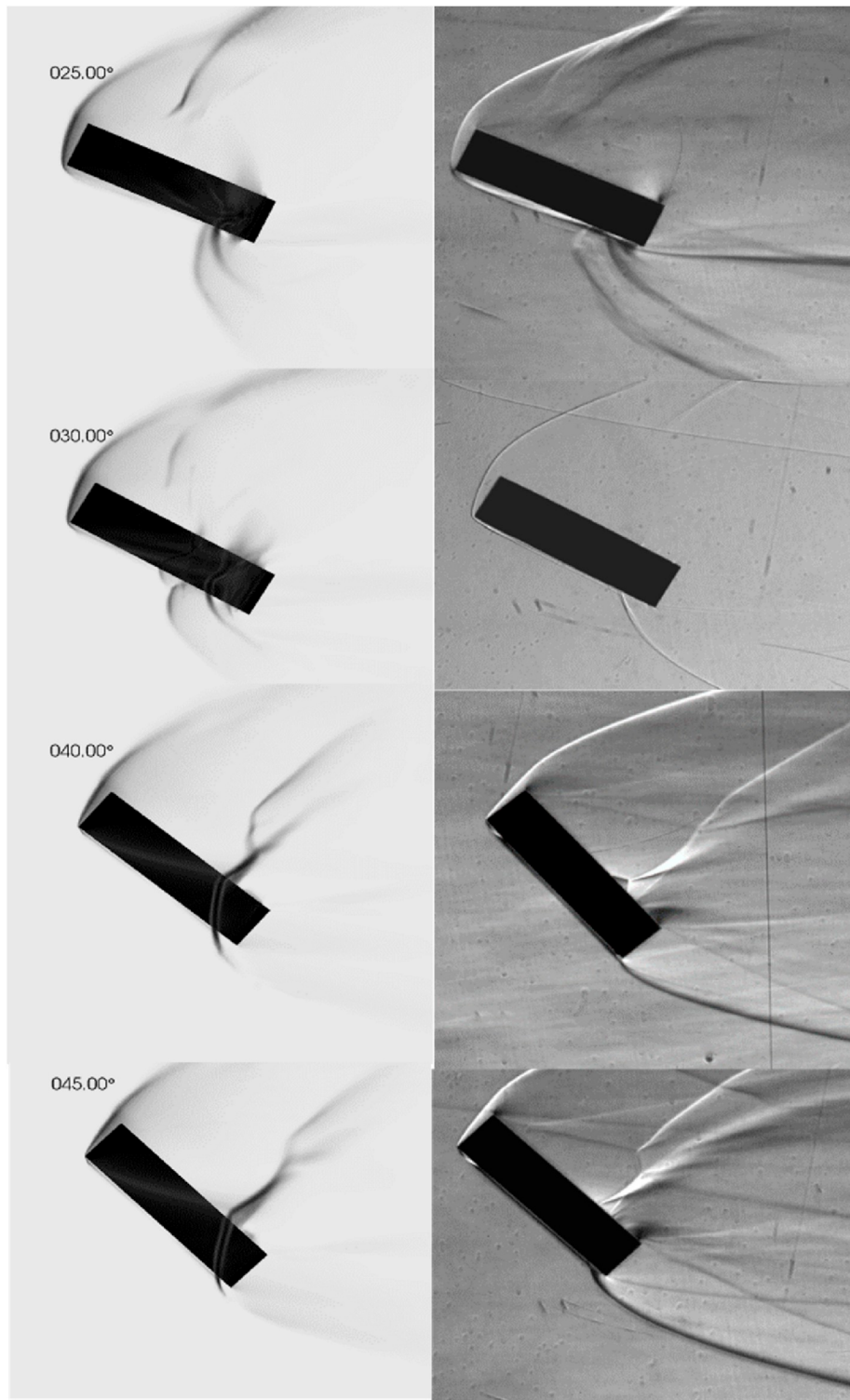


Fig. 22. Schlieren CFD (L) vs experiment (R).

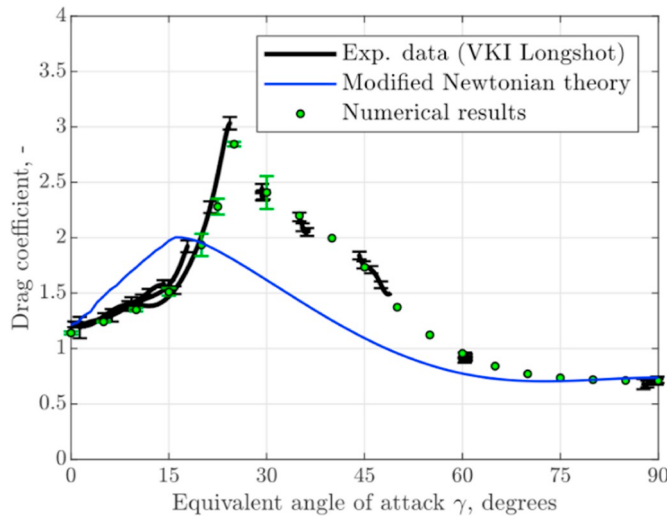


Fig. 23. Drag coefficient for a hypersonic annular ring (aspect ratio 1/4th) for different angles of attack.

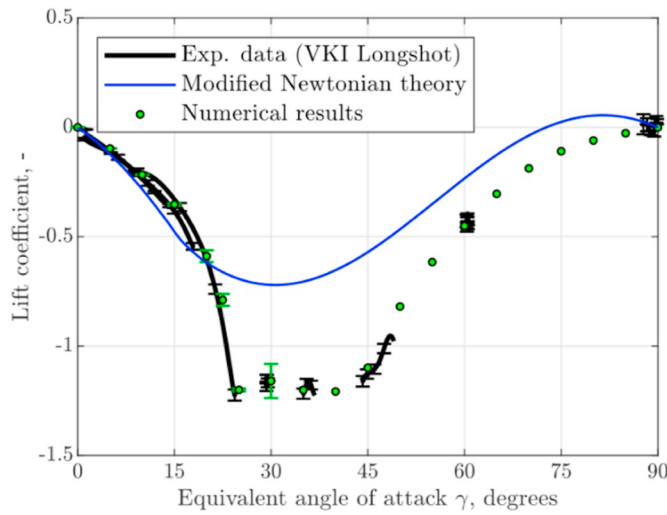


Fig. 24. Lift coefficient for a hypersonic annular ring (aspect ratio 1/4th) for different angles of attack.

Table 3
Averaged drag coefficient for the annular ring.

C_d	C_d
Experimental value	1.664
Numerical value	1.626
Discrepancy (%)	-2.3

random tumbling averaged drag coefficient (see Table 3). As for the hollow sphere, an excellent agreement between the numerical value and the experimental value is obtained for the annular ring, despite the complexity of flow (unsteady flow effects, shock interactions).

The pressure coefficient on one of the probes inside the annular ring is shown in Fig. 25, where the unsteadiness is visualised by the error bars that represents the variations of the pressure sensors, visible between 20° and 50°. Overall good agreement is observed, especially for

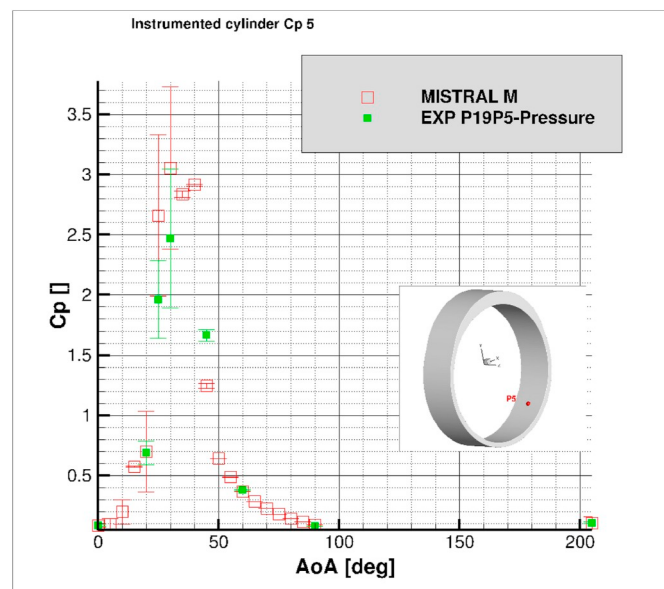


Fig. 25. Pressure coefficient on the interior of the annular ring.

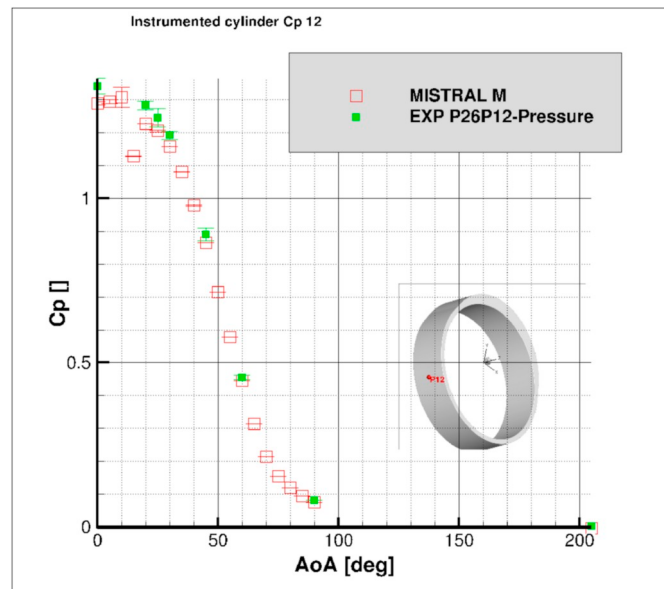


Fig. 26. Pressure coefficient on the exterior of the annular ring.

the angles of attack for which the flow is stable. Fig. 26 shows that surface pressure coefficients for one of the exterior probes matches perfectly with the experimental data.

While the annular ring is a geometrically simple object, complex unsteady flow physics with shock wave boundary layer interactions occurs, leading to locally and temporary heat fluxes and pressures that are largely exceeding the stagnation point values, pressure coefficients greater than 6 have been observed experimentally and numerically.

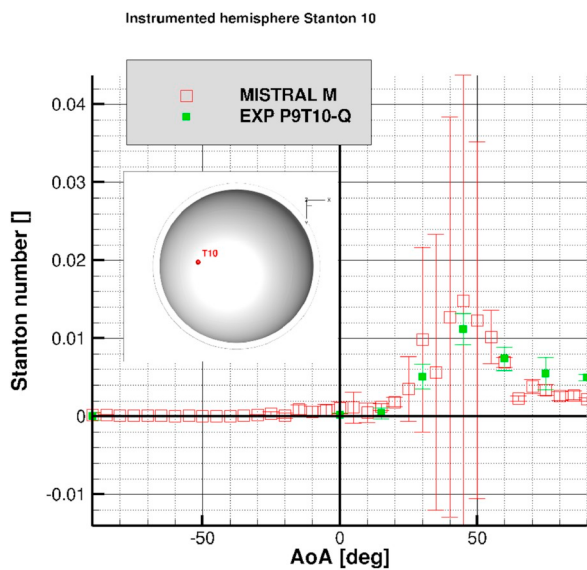


Fig. 27. Stanton number upstream point interior of the hollow sphere.

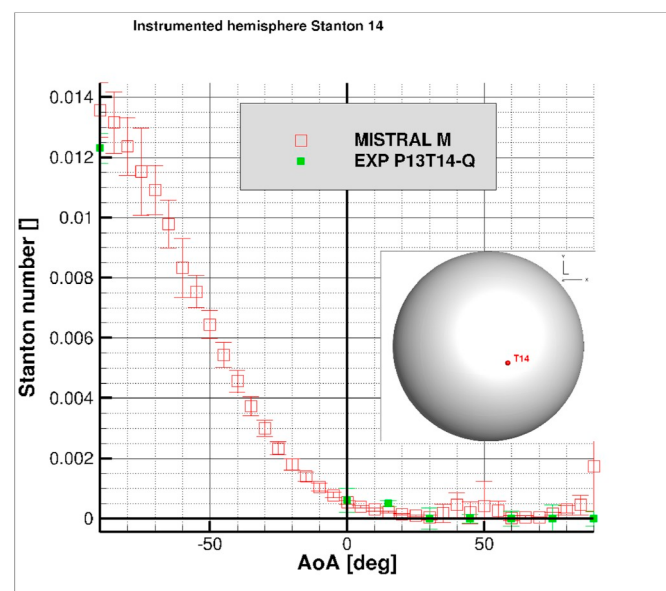


Fig. 29. Stanton number exterior of the hollow sphere.

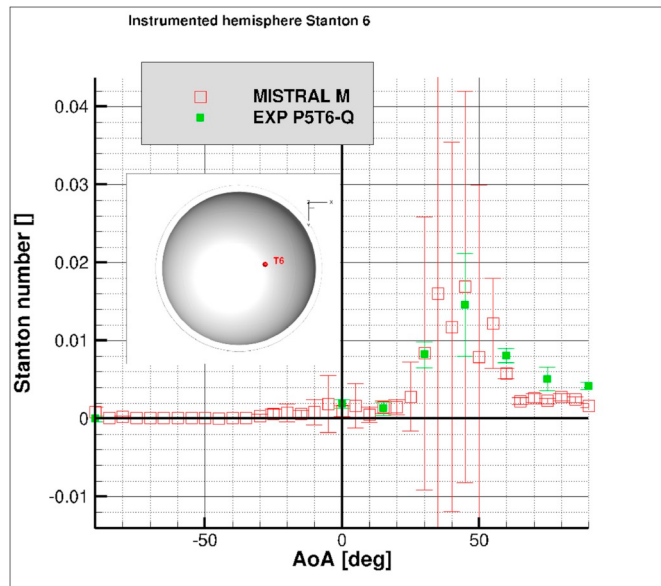


Fig. 28. Stanton number downstream point interior of the hollow sphere.

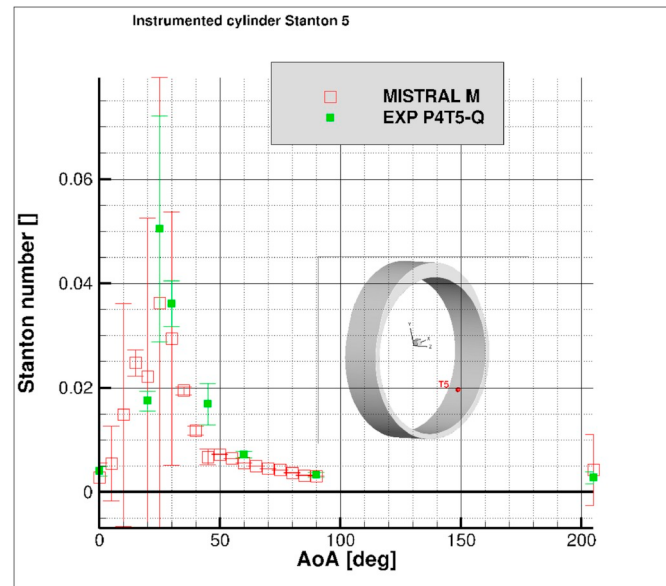


Fig. 30. Stanton on the interior of the annular ring.

4.3. Aerothermodynamics

The measured and computed Stanton numbers are presented in the figures above for the hollow sphere for some of the thermocouples (Fig. 27, Fig. 28, Fig. 29). A time averaging is applied and the variations of the signal are plotted as error bars (1 sigma). As can be seen, the trends are well captured, and therefore the surface averaged values agree rather well with estimations from the experiments. Locally discrepancies can be observed due to the very local high gradients. A slight difference in shock location or flow non-uniformity in the experiment could easily introduce large differences. It should be noted also that the

probes have been positioned in the most interesting and challenging areas, and not in the more traditional flow configurations such as the convex part of the hollow sphere, where excellent agreement on both pressure coefficient and Stanton number is observed. In addition, despite large differences in some cases, good results are obtained overall. For the purpose of DEBRISK, where both surface averaging and random tumbling averaging values are introduced in the database, the local discrepancies are believed to cancel out, and the conclusion can be made that the Longshot campaign validates the use of the MISTRAL code for the construction of the aerothermal database.

The same conclusions are valid for the Stanton numbers on the

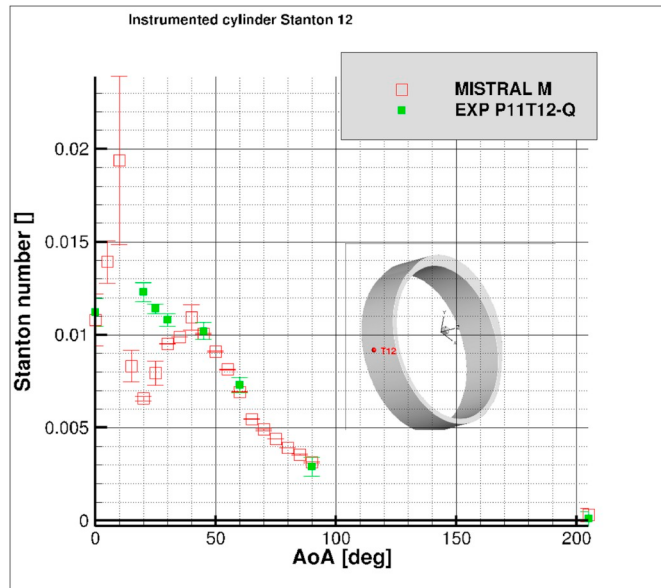


Fig. 31. Stanton on the exterior of the annular ring.

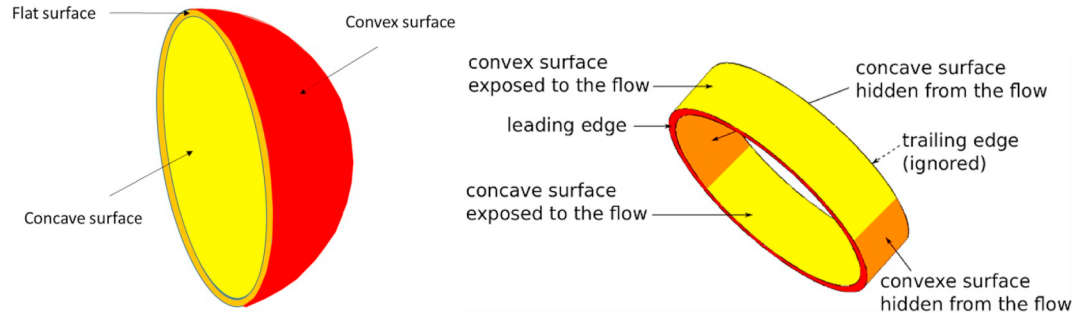


Fig. 32. Decomposition of the different surfaces.

annular ring as shown in Fig. 30 and Fig. 31.

The final integrated heat fluxes for randomly tumbling attitude are directly obtained by integrating the surface heat flux in the CFD computations. Similar quantities can be derived from the experimental data

where assumptions are necessary concerning the heat flux along the leading edges (not instrumented) and by interpolating techniques in between the instrumented locations. The figures below (from Fig. 33 to Fig. 36) show the integrated heat flux contributions for the different

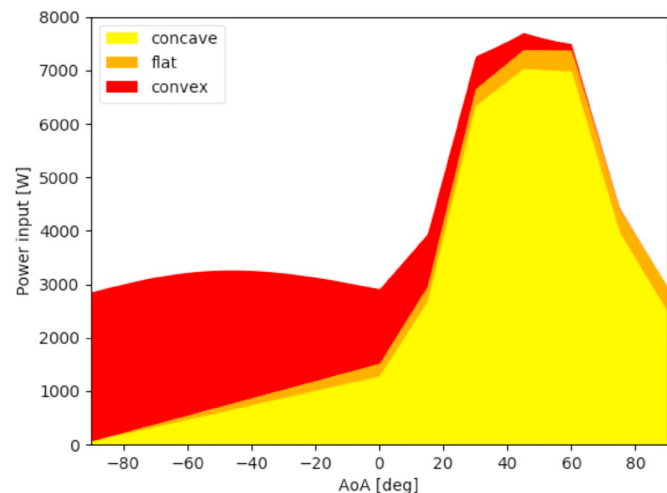


Fig. 33. Experiment: integrated heat flux versus angle of attack for hollow sphere.

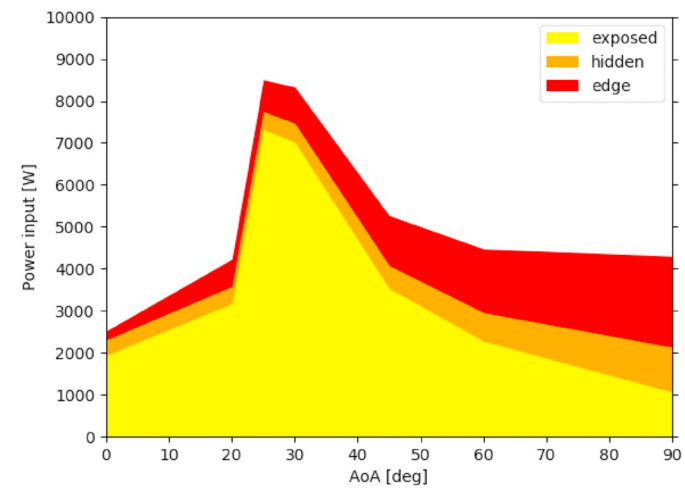


Fig. 35. Experiment: integrated heat flux versus angle of attack for annular ring.

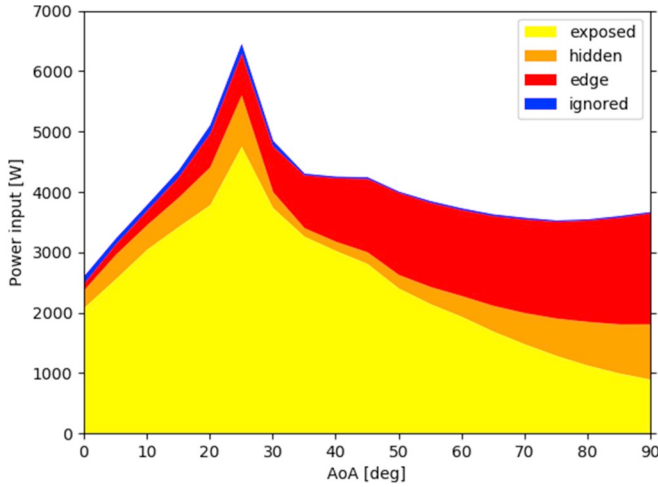


Fig. 36. CFD: Integrated heat flux distributions versus angle of attack for annular ring.

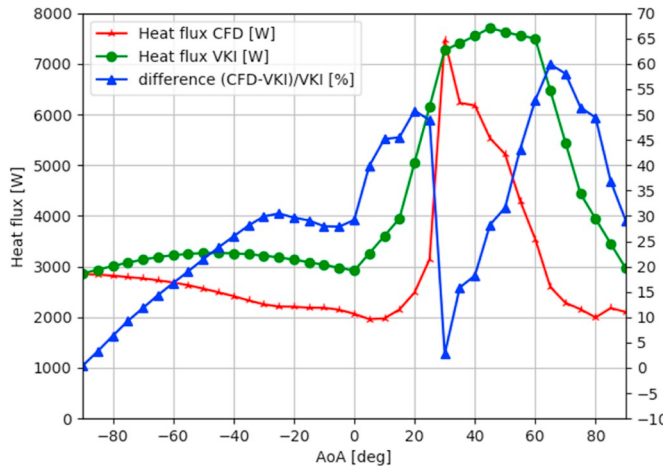


Fig. 37. Discrepancy between CFD and experiment on the integrated heat flux for the hollow sphere.

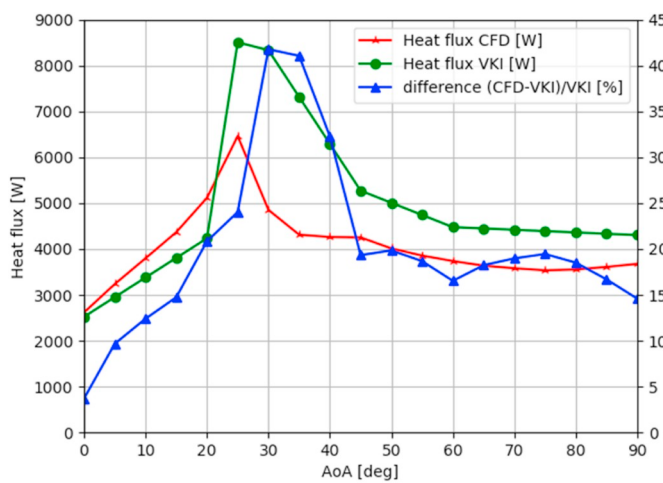


Fig. 38. Discrepancy between CFD and experiment on the integrated heat flux for the annular ring.

Table 4
Averaged heat fluxes for the hollow sphere and the annular ring.

	Hollow sphere	Annular ring
Experimental value, Q (W)	4164	4777
Numerical value, Q (W)	3053	4239
Discrepancy (%)	-26	-11

faces of the objects: concave/convex/edge for the hollow sphere and the annular ring (see Fig. 32). Overall, we can notice that the levels of the different contributions are consistent between CFD computations and experiments. Depending on the angle of attack, the face contributing the most to the integrated heat flux is not necessarily the same. Large differences between CFD and experiment can locally appear (maximum discrepancy around 50%, see Fig. 37 and Fig. 38): e.g. instabilities around 30° for the annular ring and 80° for the hollow sphere is observed, both for computations and for experiment. The individual angles have been integrated in order to obtain the random tumbling averaged heat fluxes for the hollow sphere and the annular ring (see Table 4). The numerical value is close with the experimental value for the hollow sphere (26%) and the annular ring (11%) despite the numerical difficulties, the instabilities of the flow and the experimental hypotheses to obtain this type of values.

4.4. Sting effects

The effect of the support has been investigated. For only a limited number of angles of attack since in those cases the spherical mesh approach cannot be used. Here again, very good qualitative results have been obtained when comparing, at two different times, the experimental Schlieren images with numerical rebuilding (see Fig. 39). For the hollow sphere case the quantitative results on the Stanton number results were in better agreement when modelling the sting effect (increased heating in the interior of the sphere has been observed when including the support in the computations).

5. Conclusion

A new and an innovative methodology has been implemented in order to extend the number of available preliminary shapes within DEBRISK with the goal to deal accurately with the atmospheric reentry of more realistic objects. With these new complex shapes, the pre-fragmentation of the satellite, performed by the user, is now more representative to the real geometry of the spacecraft. The database generated is able to deal with a large variety of new topologies.

This methodology was also validated by setting up an important aerothermodynamics experimental campaign, where a good agreement has been observed between experiments and numerical predictions.

Acknowledgments

All this work has been supported by the CNES contracts (170771/00, 180348/00, 170990/00), in the frame of the DEBRISK project.

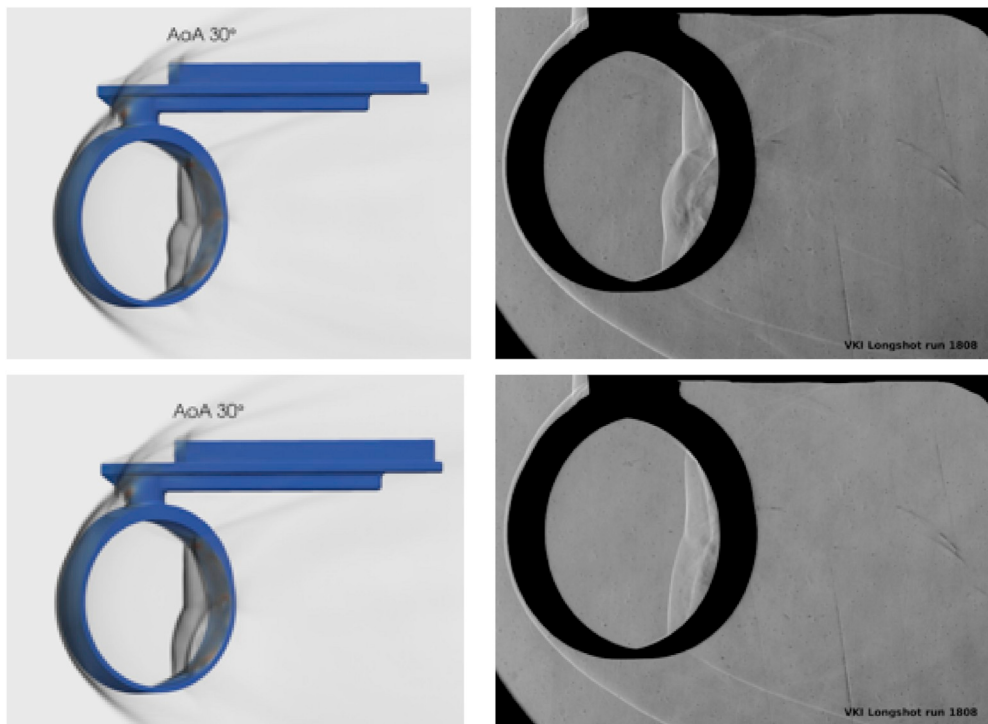


Fig. 39. Sting influence.

References

- [1] Satellite Catalog Data, Space Track Organization, 2016, <http://www.space-track.org>.
- [2] H. Klinkrad, Space Debris, Models and Risk Analysis, Springer-Verlag, 3540376747, 2006.
- [3] Space Debris Mitigation Guidelines of the Committee on the Peaceful Uses of Outer Space, United Nations, Office For Outer Space Affairs, Vienna, January, 2010.
- [4] <https://www.iso.org/standard/72383.html>.
- [5] NASA Safety Standards, Guidelines & Assessment Procedures for Limiting Orbital Debris, (August 1995) Technical Report NSS-1740.14.
- [6] NASA Technical Standard, Process for Limiting Orbital Debris, NASA-STD 8719.14, Revision B, (April 2019).
- [7] ESA Space Debris Mitigation Compliance Verification Guidelines, ESSB-HB-U-002, February 2015.
- [8] Irene Pontijas Fuentes, Upgrade of ESA's debris risk assessment and mitigation analysis (DRAMA) tool: spacecraft entry survival analysis module, *Acta Astronaut.* 158 (May 2019) 148–160.
- [9] P. Omaly, C. Magnin Vella, S. Galera, DEBRISK, CNES tool for re-entry survivability prediction: validation and sensitivity analysis, IAASS, 2013.
- [10] P. Omaly, J. Annaloro, DEBRISK V3: CNES Tool Evolutions for Re-entry Risk Analysis, IAASS, 2019.
- [11] R.D. Klett, Drag Coefficients and Heating Ratios for Right Circular Cylinders in Free Molecular and Continuum Flow from Mach 10 to 30, SC-RR-64-2141, Sandia Corporation, Dec.1964.
- [12] C. Ostrom, C. Sanchez, ORSAT Modelling and Assessment, 4th International Workshop on Space Debris Reentry, (2018) Darmstadt.
- [13] R. Kanzler, et al., Upgrade of DRAMA's Spacecraft Entry Survival Analysis Codes, 4th International Workshop on Space Debris Reentry, Darmstadt, 2018.
- [14] G. Grossir, B. Dias, O. Chazot, T.E. Magin, High temperature and thermal non-equilibrium effects on the determination of free-stream flow properties in hypersonic wind tunnels, *Phys. Fluids* 30 (126102) (2018) 1–13.
- [15] G. Grossir, D. Puorto, Z. Ilich, S. Paris, O. Chazot, S. Rumeau, M. Spel, J. Annaloro, Aerodynamic characterization of space debris in the VKI Longshot hypersonic tunnel using a free-flight measurement technique, International Conference on Flight Vehicles, Aerothermodynamics and Re-entry Missions and Engineering (FAR), Monopoli, Italy, 201930 Sept – 3 October.